Mechanical Systems and Signal Processing 112 (2018) 129–146

Contents lists available at ScienceDirect

Mechanical Systems and Signal Processing

journal homepage: www.elsevier.com/locate/ymssp

Effect of fractionally damped compliance elements on amplitude sensitive dynamic stiffness predictions of a hydraulic bushing

Luke Fredette, Rajendra Singh *

Acoustics and Dynamics Laboratory, Smart Vehicle Concepts Center, Department of Mechanical and Aerospace Engineering, The Ohio State University, Columbus, OH 43210, USA

ARTICLE INFO

Article history:
Received 17 January 2017
Received in revised form 5 April 2018
Accepted 15 April 2018

Keywords:
Nonlinear system simulation
Fractional calculus viscoelasticity
Dry friction
Hydraulic devices
Vibration control

ABSTRACT

Hydraulic bushings exhibit significant amplitude dependent behavior which cannot be captured with the linear time-invariant system theory. Accordingly, Fredette et al. (2016) have proposed a nonlinear model, but the amplitude sensitivity has not been adequately described as it is affected by multiple inherent design features. To further improve the predictive capability of nonlinear models, this article extends the prior work by including two key dissipation effects within the (elastomeric) fluid compliance chambers. First, the conventional fluid compliance element is replaced by an equivalent mechanical spring representing the nonlinear elasticity of the pumping chambers. Fractional calculus based and friction-type damping elements are added in parallel to the nonlinear spring elements of pumping chambers. Second, improved quasi-linear models are proposed at four sinusoidal excitation amplitudes, demonstrating amplitude sensitivity in model parameters. Third, new nonlinear models are proposed and numerically simulated, predicting dynamic stiffness magnitudes and loss angles at multiple excitation amplitudes. The sensitivity of dynamic properties to the fractional and frictional damping parameters is qualitatively evaluated. Finally, both quasi-linear and nonlinear models are experimentally validated and are found to be superior to the ones in the literature.

1. Introduction

In a recent paper, Fredette et al. [1] developed hydraulic bushing models with multiple nonlinear elements including a measurement based compliance model for the elastomeric chambers. While the previous article offered new insight into the physics of these devices, the results of [1] suggest that there is room for further improvement in dynamic stiffness predictions which are sensitive to the excitation amplitude. A major deficiency of prior work [1] has been a lack of damping formulation for the compliance chambers (containing the hydraulic fluid) although the elastomeric material exhibits significant viscoelasticity which could influence the amplitude sensitive dynamics. Several investigators have studied the low-frequency dynamics of hydraulic bushings, but the majority of the literature has employed the linear time-invariant system principles [2–5], despite significant amplitude sensitivity observed in such devices [1,6–8]. A few researchers have proposed amplitude sensitive models, using either a quasi-linear or nonlinear approach. For instance, Svensson and Håkansson [6]

---

* Corresponding author.
E-mail address: singh.3@osu.edu (R. Singh).

https://doi.org/10.1016/j.ymssp.2018.04.031

developed a hydraulic bushing model which included a nonlinear elastic element for the rubber path, but used the linear system principles for the fluid path. Chai et al. [7] proposed a model with a nonlinear fluid resistance term, which introduced significant amplitude sensitivity. However, this study was limited to a laboratory device which replicated only certain behavior of a production device. A recent experimental study by Fredette et al. [8] identified pressure dependent compliance behavior in the fluid system of a production bushing, which led to improved models with both nonlinear fluid resistance and chamber compliance elements [1,8], but provided limited analysis of the damping.

The major goal of this article is to significantly extend the prior formulation [1] by introducing fractional calculus based viscoelasticity and additional nonlinear elements. New or improved models of this study are expected to enhance modeling capabilities and to better understand the underlying physics of hydraulic bushings since they often have complex designs with interacting features. In particular, the effect of frictionally and fractionally damped compliance chambers will be studied and a new technique for analyzing this potentially nonlinear feature will be proposed. The literature on this topic is limited even though the fractional calculus based constitutive laws have been shown to represent the viscoelasticity of many elastomeric materials in a compact, accurate, and physically meaningful way [9–15]. Such viscoelastic behavior should be present in many types of elastomeric isolators and hydraulic bushings. In particular, the approach of the current article is inspired, in part, by the prior work of Sjoberg and Kari [11] who combined nonlinear elasticity, fractional viscoelasticity, and smoothened dry friction damping to mimic the dynamic behavior of a carbon black filled rubber isolator. Instead, the focus of this article will be on the damping effects of elastomeric materials on certain fluid system elements in a typical hydraulic bushing that is commonly employed in vehicle suspension systems [16,17].

2. Problem formulation

The scope of this article is on a class of production grade hydraulic bushings that is schematically described via a baseline lumped parameter system model in Fig. 1; it is equivalent to the formulation of [1]. Steady-state sinusoidal excitation and transmitted force response are used to estimate the dynamic stiffness $\tilde{K}$ in the example case used in [1]. Fig. 1 shows a schematic of the component split into two parallel force transmission paths, where $x(t) = (x_a/2)\sin(2\pi\Omega t)$ is the inner sleeve's displacement excitation, with peak-to-peak amplitude x_a and frequency Ω with units of Hz. The forces transmitted to the outer sleeve through the rubber and fluid paths are denoted F_r and F_f, respectively. Here, p_1 and p_2 represent the dynamic pressures in each pumping chamber, while q_i denotes the volume flow rate in the inertial track. The fluid resistance and inertance of the inertia track are given by R_i and I_i, and C_f is the fluid compliance of the pumping fluid, uniform in both chambers. The effective pumping area of the inner sleeve is given by A_x. Finally, the rubber path stiffness is denoted k_r, with rubber path damping force defined in a function form as $g_r(x, \dot{x})$. Typically, viscous damping would be employed, implying that $g_r(x, \dot{x}) = \eta_r \dot{x}$, where η_r is the viscous damping coefficient.

The governing equations of the fluid system are given by the continuity equations for each pumping chamber,

$$C_f \dot{p}_1(t) = A_x \dot{x}(t) - A_c \dot{y}_1(t) - q_i(t), \tag{1a}$$

$$C_f \dot{p}_2(t) = -A_x \dot{x}(t) - A_c \dot{y}_2(t) + q_i(t), \tag{1b}$$

and the momentum equation for the inertial track,

$$I_i \dot{q}_i(t) = p_1(t) - p_2(t) - R_i q_i(t). \tag{1c}$$

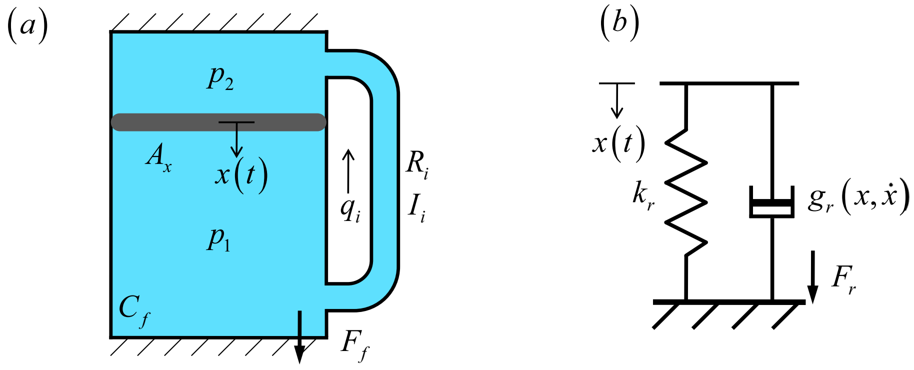

Fig. 1. Schematic of the hydraulic bushing where the (a) fluid path and (b) rubber path subsystems correspond to the analysis of prior work [1]. Here, $x(t)$ is the inner sleeve's displacement excitation while F_r and F_f are the forces transmitted to the outer sleeve through the rubber and fluid paths, respectively. The pressures in each pumping chamber are denoted by p_1 and p_2, and q_i is the volume flow rate in the inertial track. The fluid resistance and inertance of the inertia track are given by R_i and I_i, and C_f is the combined fluid compliance of the pumping fluid and each chamber. A_x is the effective pumping area of the inner sleeve. The rubber path stiffness is denoted k_r, with damping force $g_r(x, \dot{x})$.

The transmitted force through each path are calculated as,

$$F_f(t) = A_x(p_1(t) - p_2(t)), \tag{2}$$

$$F_r(t) = k_r x(t) + g_r(x(t), \dot{x}(t)), \tag{3}$$

and the total transmitted force is, $F_T(t) = F_f(t) + F_r(t)$.

The focus of this article is on the quantification of damping effects that result from the deformation of the pumping chamber walls. Accordingly, a more detailed system description is required in order to capture the chamber damping effects and overcome the deficiencies of prior work [1]. A new computational strategy would also be necessary to incorporate fractional and friction damping into the new model. The new configuration is proposed in Fig. 2, where all previously defined symbols retain their meaning. Additionally, A_c is the effective piston area of the pumping chamber, and the spring coefficient k_c and effective mass m_c represent the elastic and inertial properties of the compliance chamber walls.

Two types of modeling methods are employed in this article to give robust treatment to the amplitude sensitivity which may be observed in hydraulic bushings [1], and a description of each model used in this article is given in Table 1. Quasi-linear models are linearized, transfer function type models which employ a set of empirical parameters that depend on the excitation and are determined from dynamic measurements for a given excitation type and amplitude. The quasi-linear model used in prior work is designated model I [1] while the new one (developed later in Section 4) is designated II. The strength of this approach is that good accuracy can be achieved from curve-fitting, but on the other hand experiments must be conducted for every excitation type and amplitude of interest. Thus the quasi-linear model's utility is limited, as it may be used to assess whether the configuration and order of the model is suitable to capture the linearized dynamics of the device. Further, nonlinear models contain nonlinear elements which may capture amplitude dependent system properties directly in the time domain. The nonlinear model used in prior work is designated III [1] while variations of the new one (developed later in Section 5) are designated IV-0, IV-1, and IV-2. These require a more precise quantitative understanding of the underlying physics than do quasi-linear models, but predict amplitude sensitive dynamics with a single, unified set of parameters. Dynamic predictions which agree with measurements over a range of excitation amplitudes and frequencies suggest a refined characterization of the nonlinear dynamics of hydraulic bushings. Thus a comparative, critical assessment of the competing models naturally flows from modeling insights and experimental validation, revealing the limitations of prior models.

The particular objectives of this article are to (1) develop refined quasi-linear models which simulate the pumping chamber damping effects leading to amplitude-dependent dynamic stiffness behavior, (2) Improve the nonlinear models of prior paper [1] by including fractional calculus and dry-friction type damping elements in the pumping chambers, and (3) validate the predictions of the new models against dynamic stiffness measurements while critically assessing the strengths and limitations of each model. The significance of chamber damping is therefore demonstrated by the improved performance of

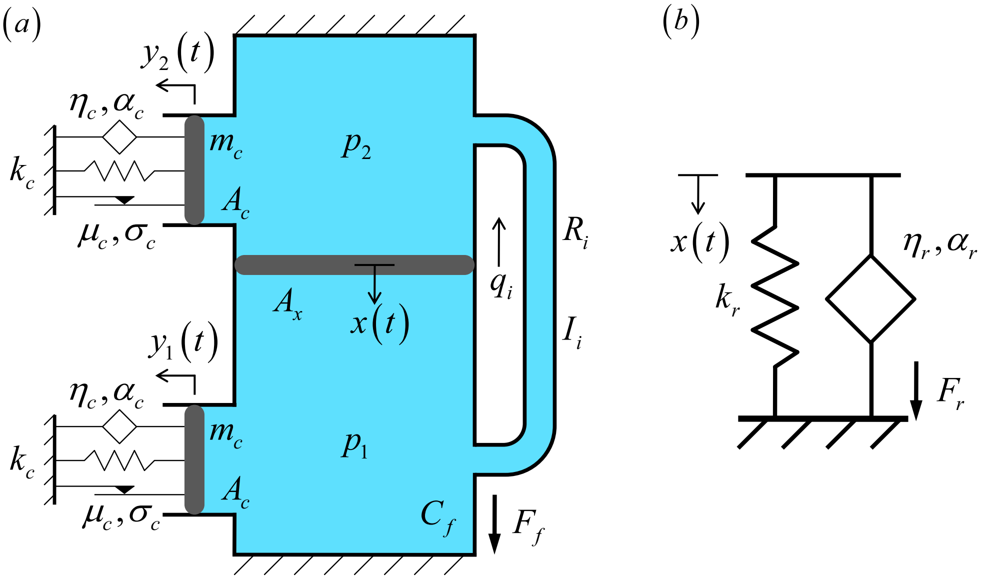

Fig. 2. Schematic of new quasi-linear and nonlinear models of hydraulic bushing with parallel fluid path (*a*) and rubber path (*b*) subsystems. Here, A_c is the effective pumping area of the pumping chambers (assumed to be identical). The spring coefficient k_c and effective mass m_c represent the elastic and inertial properties of the pumping chamber walls. The fractional damping coefficient and order of the pumping chamber are given by η_c, α_c, respectively. The friction coefficient is given by μ_c with smoothing parameter σ_c. The rubber path stiffness is denoted k_r, with fractional rubber damping $g_r(x, \dot{x}) = \eta_r D_t^{\alpha_r}(x)$. For other symbols, refer to Fig. 1.

Table 1
Description of quasi-linear (QL) and nonlinear (NL) models used in this article and comparison with prior work [1]. See Fig. 2 for the system description and symbols.

Model	Type	From [1] (Fig. 1)	New (Fig. 2)	Description	Rubber Path $g_r(x,\dot{x})$	Pumping Chamber $g_c(y,\dot{y})$
I	QL	×		Undamped pumping chambers	$\eta_r\dot{x}$	0
II	QL		×	Fractionally damped pumping chamber	$\eta_r D_t^\alpha(x)$	$\eta_c D_t^\alpha(y)$
III	NL	×		Nonlinear $R_i(q)$ and $C(p)$ elements and undamped pumping chambers	$\eta_r D_t^\alpha(x)$	0
IV-0	NL		×	Undamped, equivalent mechanical spring in place of $C(p)$	$\eta_r D_t^\alpha(x)$	0
IV-1	NL		×	Fractional and friction-type damping elements for pumping chamber with constant A_x	$\eta_r D_t^\alpha(x)$	$\eta_c D_t^\alpha(y) + \mu_c \tanh(\sigma_c\dot{y})$
IV-2	NL		×	Fractional and friction chamber damping elements with QL $A_x = A_x(x_a)$	$\eta_r D_t^\alpha(x)$	$\eta_c D_t^\alpha(y) + \mu_c \tanh(\sigma_c\dot{y})$

models II and IV over models I and III (which are both directly from [1]) respectively, when compared with measurements. The scope of this article is limited to component-level, uniaxial, steady-state harmonic analysis of the example case up to a 50 Hz bandwidth with peak-to-peak displacement amplitudes of 0.1, 0.5, 1.0, and 2.0 mm.

3. Fractional damping formulation

Fractional dampers are governed by fractional calculus constitutive laws[9–15]. In particular, the damping force in each fractional damper is given by $F(t) = \eta D_t^\alpha z(t)$, where $z(t)$ is the displacement of the element, α is the fractional order, and D_t^α is a differential operator defined,

$$D_t^\alpha(\cdot) = \frac{d^\alpha}{dt^\alpha}(\cdot). \tag{4}$$

It should be noted that viscous damping is a special case of fractional damping where $\alpha = 1$, and structural (material) damping is the case when $\alpha = 0$ and the coefficient η is purely imaginary. In general, the Caputo definition of a fractional derivative is the Cauchy integral [9,10],

$$D_t^\alpha z(t) = \frac{1}{\Gamma(1-\alpha)} \int_x^0 (t-\tau)^{-\alpha} \frac{dz}{dt} d\tau, \tag{5}$$

which has the convenient Laplace transform, $\mathcal{L}\{D_t^\alpha z(t)\} = s^\alpha Z(s)$. This facilitates the frequency-domain quasi-linear models (as developed in Section 4). For numerical integration, however, the Caputo definition is prohibitively cumbersome. Therefore the numerical, time-domain analysis of Section 5 uses the Grünwald-Letnikov definition [9,10],

$$D_t^\alpha z(t) = \lim_{h\to 0} h^{-\alpha} \sum_{j=0}^{\infty} \binom{\alpha}{j} (-1)^j z(t - jh), \tag{6}$$

where h is the length of one time-step. This formulation is easily converted to a difference equation,

$$D_t^\alpha z(t_0) \approx h^{-\alpha} \sum_{j=0}^{N_j} \binom{\alpha}{j} (-1)^j \bar{z}[N_j - j], \tag{7}$$

where square brackets denote indexing a discrete vector, the overbar denotes a history variable such that $\bar{z}[j]$ is a vector of the history of $z(t)$, sampled with a period of h, such that $\bar{z}[0] = z(t_0 - N_j h)$ and $\bar{z}[N_j] = z(t_0)$. Eq. (7) accurately approximates the fractional derivative of the signal at time t_0, given a sufficiently large number of history points, N_j, and a sufficiently small h.

4. Development of a quasi-linear model (II)

The quasi-linear model framework utilizes a linearized model with empirical parameters that discretely vary with excitation amplitude, and the system description of Fig. 2 is employed to extend the prior work [1]. The fractional damping coefficient and order of the pumping chamber are given by η_c, α_c, respectively. The dry friction element is characterized by a coefficient (μ_c) and smoothing parameter (σ_c); it will be discussed in more detail later since it is a nonlinear element and cannot therefore be captured in the quasi-linear model.

The general governing equations of a refined (and yet a more general) fluid system of Fig. 2 are given by

$$C_f \dot{p}_1 = A_x \dot{x} - A_c \dot{y}_1 - q_i, \tag{8a}$$

$$C_f\dot{p}_2 = -A_x\dot{x} - A_c\dot{y}_2 + q_i, \tag{8b}$$

$$m_c\ddot{y}_1 = A_cp_1 - k_cy_1 - g_c(y_1, \dot{y}_1), \tag{8c}$$

$$m_c\ddot{y}_2 = A_cp_2 - k_cy_2 - g_c(y_2, \dot{y}_2), \tag{8d}$$

$$I_i\dot{q}_i = p_1 - p_2 - R_iq_i. \tag{8e}$$

The chamber and rubber path damping forces in model II (corresponding to Fig. 2) are defined using the fractional derivative,

$$g_c(y, \dot{y}) = \eta_c D_t^{\alpha_c} y, \tag{9}$$

$$g_r(x, \dot{x}) = \eta_r D_t^{\alpha_r}(x). \tag{10}$$

Certain simplifications enhance the tractability of quasi-linear and nonlinear analyses of these equations. For instance, it has been previously demonstrated that the compliance of the fluid medium is much smaller than the compliance associated with the container [1,8]; this suggests that $C_f \approx 0$ would be a reasonable assumption. Finally, since the upper frequency of interest (50 Hz) is relatively low, the effect of chamber wall mass is negligible, $m_c \approx 0$. The computational implications of this assumption for nonlinear models will be discussed in Section 5.

The quasi-linear analysis is based on the linear-time-invariant system theory, so there is an inherent assumption that any nonlinearity present is weak. Using linearized (constant) model parameters, the dynamic stiffness of model II is defined in the Laplace domain as,

$$\tilde{K}_{II}(s) = \frac{\tilde{F}_T}{X}(s) = \frac{\tilde{F}_r}{X}(s) + \frac{\tilde{F}_f}{X}(s), \tag{11}$$

where $X(s) = \mathcal{L}\{x(t)\}$. The $\tilde{K}(s)$ transfer function is derived,

$$\tilde{K}_{II}(s) = \frac{B_{10}s^{2+\alpha_r} + B_9s^{2+\alpha_c} + B_8s^2 + B_7s^{1+\alpha_r} + B_6s^{1+\alpha_c} + B_5s + B_4s^{\alpha_c+\alpha_r} + B_3s^{\alpha_r} + B_2s^{\alpha_c} + B_1}{s^2 + B_{13}s + B_{12}s^{\alpha_c} + B_{11}}, \tag{12a}$$

where

$$B_1 = \frac{2k_ck_r}{I_iA_c^2}, \quad B_2 = \frac{2\eta_ck_r}{I_iA_c^2}, \quad B_3 = \frac{2k_c\eta_r}{I_iA_c^2}, \tag{12b, c, d}$$

$$B_4 = \frac{2\eta_c\eta_r}{I_iA_c^2}, \quad B_5 = \frac{R_i}{I_i}\left(k_r + \frac{2A_x^2k_c}{A_c^2}\right), \quad B_6 = \frac{2R_iA_x^2\eta_c}{I_iA_c^2}, \tag{12e, f, g}$$

$$B_7 = \frac{R_i\eta_r}{I_i}, \quad B_8 = \left(k_r + \frac{2A_x^2k_c}{A_c^2}\right), \quad B_9 = 2\eta_c\frac{A_x^2}{A_c^2}, \tag{12h, i, j}$$

$$B_{10} = \eta_r, \quad B_{11} = \frac{2k_c}{I_iA_c^2}, \quad B_{12} = \frac{2\eta_c}{I_iA_c^2}, \quad B_{13} = \frac{R_i}{I_i}. \tag{12k, l, m, n}$$

Thus model II has ten independent physical parameters: $A_x, k_c, \eta_c, \alpha_c, k_r, \eta_r, \alpha_r, I_i, R_i$, and A_c, compared with only six physical parameters in model I. Also, the transfer function of model I was third-order system over second-order system with 6 coefficients, whereas Model II is has a fractional-order lead term in the numerator and 13 coefficients.

With a reasonable initial guess, the parameters are empirically optimized using measured dynamic stiffness spectra at several excitation amplitudes [1] and a Levenberg-Marquardt least-squares curve fitting algorithm [17]. Model II's parameters are tabulated and normalized by the baseline values (corresponding to a 0.1 mm excitation amplitude) in Table 2 to evaluate each one's amplitude sensitivity. It may be observed that three parameters (A_c, k_c, and η_c) parameters are only found in the ratios given by k_c/A_c^2 or η_c/A_c^2. Specifying all three parameters is therefore redundant, and thus k_c and η_c are scaled such that A_c remains constant for all amplitudes. Figs. 3 and 4 compare the calculated dynamic stiffness spectra of model I [1] and model II at each amplitude with the measurement in terms of magnitude and phase, respectively. To better assess models, Table 3 compares the root mean squared (RMS) error of the two quasi-linear models (I and II) defined as,

$$\varepsilon_I = \frac{1}{K_0}\sqrt{\frac{1}{N_\Omega}\sum\nolimits_\Omega \left(\tilde{K}_I(\Omega) - \tilde{K}_M(\Omega)\right)^2} \tag{13a}$$

Table 2
Amplitude sensitivity in the parameters of quasi-linear model II. Each parameter is normalized by the baseline value at 0.1 mm peak-to-peak excitation. See Figs. 1 and 2 for symbols.

Parameter	Peak-to-peak amplitude (x_a)			
	(baseline) 0.1 mm	0.5 mm	1.0 mm	2.0 mm
A_x (m^2)	1.00	0.99	1.02	1.19
k_c (N/m)	1.00	1.04	0.94	0.64
η_c (Ns$^{\alpha_c}$/m)	1.00	0.36	0.44	0.42
α_c	1.00	1.38	1.28	1.15
k_r (N/m)	1.00	1.00	0.98	0.95
η_r (Ns$^{\alpha_r}$/m)	1.00	0.85	0.83	1.14
α_r	1.00	0.80	0.67	0.52
I_i (kg/m^4)	1.00	0.95	0.88	0.65
R_i (kg/m^4 s)	1.00	1.73	2.16	2.08
A_c (m^2)	1.00	1.00	1.00	1.00

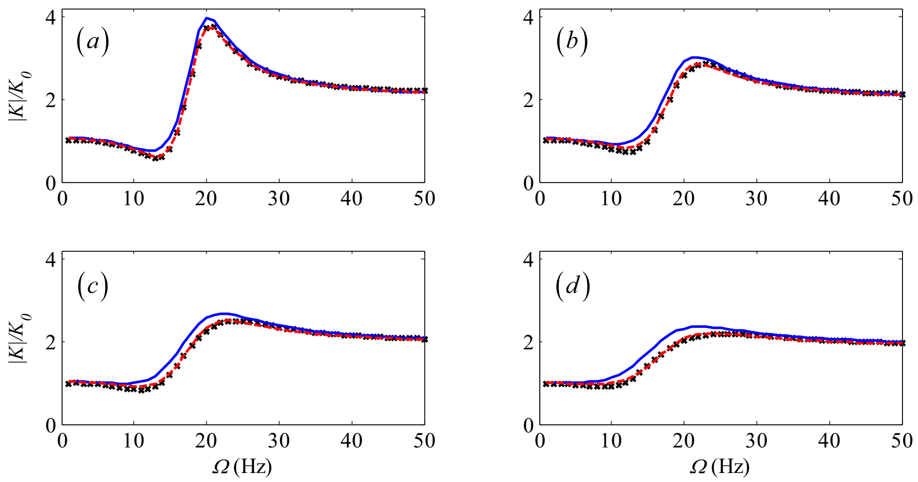

Fig. 3. Dynamic stiffness magnitudes showing improved accuracy of new quasi-linear models compared with measurement at (*a*) 0.1 mm, (*b*) 0.5 mm, (*c*) 1.0 mm, and (*d*) 2.0 mm peak-to-peak excitation amplitudes. Key: × – measurement; —— – model I [1]; - - - – model II.

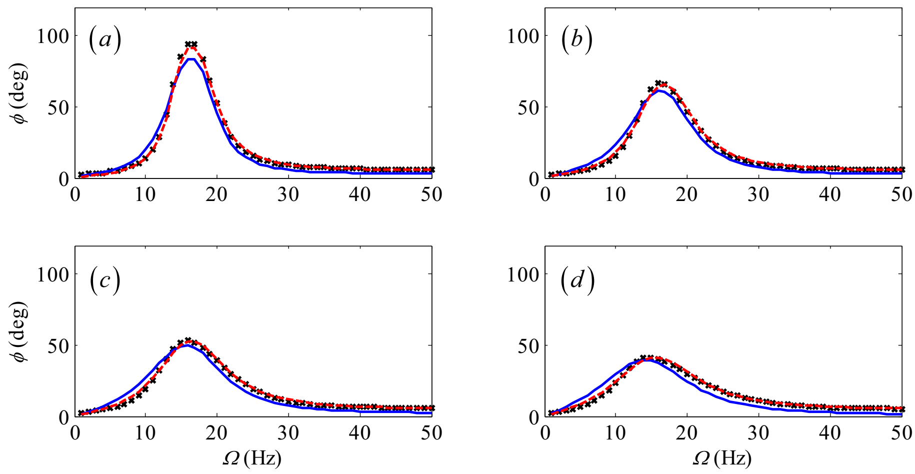

Fig. 4. Loss angles showing improved accuracy of new quasi-linear models compared with measurement at (*a*) 0.1 mm, (*b*) 0.5 mm, (*c*) 1.0 mm, and (*d*) 2.0 mm peak-to-peak excitation amplitudes. Key: × – measurement; —— – model I [1]; - - - – model II.

Table 3
Errors in the quasi-linear models with respect to measured dynamic stiffness spectra, revealing a substantial improvement in accuracy.

Model	RMS error at peak-to-peak amplitude (x_a)			
	0.1 mm	0.5 mm	1.0 mm	2.0 mm
Model I, from [1]	20.28%	18.29%	18.57%	20.45%
Model II	3.77%	5.33%	4.67%	4.10%

$$\varepsilon_{II} = \frac{1}{K_0}\sqrt{\frac{1}{N_\Omega}\sum\nolimits_\Omega (\tilde{K}_{II}(\Omega) - \tilde{K}_M(\Omega))^2}, \tag{13b}$$

using model II as an example where $\tilde{K}_M(\Omega)$ is the measured dynamic stiffness spectrum, N_Ω is the number of frequencies considered, and K_0 is the static stiffness. Observe that model II achieves a dramatic improvement in accuracy over model I [1], suggesting that the higher- and fractional-order dynamics which result from fractional calculus viscoelastic elements are necessary (or at least appropriate) to describe the measured behavior.

Several insights emerge from the quasi-linear models when the amplitude dependence of each parameter is studied. First, it is apparent that certain parameters are much more amplitude sensitive than others, indicating that not all nonlinearities in the system are weak; for instance, R_i, η_c, and α_r all change by a factor of two between the minimum and maximum amplitudes while k_r, η_r, and A_x vary by less than 20%. Second, certain parameters tend to interact in ways which obfuscates their true nature from a curve-fitting analysis. For example, the denominator natural frequency is related to k_c/I_i. While the curve-fitting procedure is effective at locating the value of the k_c/I_i ratio, it may tend to target either the k_c or I_i parameter to do so. Though the inertance should be relatively insensitive to changes in amplitude [1], the quasi-linear model shows a decrease in I_i by 35%, suggesting that the numerical procedure may have arbitrarily reduced I_i rather than increasing k_c. The resulting quasi-linear model parameters may not reflect the true amplitude sensitive physics in the device, but this would be difficult to verify in the quasi-linear model framework. A time-domain approach which directly captures the nonlinearities in the system is needed to better predict the amplitude sensitivity and thereby to understand the governing physics of this device.

5. Development of the nonlinear model (IV)

5.1. Nonlinear elements

Two nonlinear elements employed in model IV are inherited from the prior nonlinear model (III) [1]. The fluid resistance element, $R_i(q_i)$, assumes turbulent flow in the inertial track where β_i captures the geometric and fluid properties of the inertial track [1,7,18],

$$R_i(q_i) = \xi_{R_i}\beta_{R_i}|q_i|^{0.75}. \tag{14}$$

Here, $\xi_{R_i} > 1$ is added as an empirical correction factor to account for well-known entrance/exit effects, bends in the channel, and other losses [19]. A nonlinear fluid compliance element has been used [1,8] to capture the elastic behavior of the pumping chambers where the β_C coefficients are experimentally determined, $C(p) = 3\beta_{C3}p^2 + 2\beta_{C2}p + \beta_{C1}$. While this formulation proved useful in prior analysis, an equivalent, nonlinear, mechanical spring allows for a more flexible modeling framework.

To establish equivalence with the compliance model, the nonlinear spring must satisfy the volume relation, from which fluid compliance is derived:

$$V_c(p) = \beta_{C3}p_c^3 + \beta_{C2}p_c^2 + \beta_{C1}p_c + \beta_{C0} = V_{c0} + A_c y_c, \tag{15}$$

where V_{c0} is the volume of a single pumping chamber at rest with a static pressure, p_0. Ignoring damping forces (as in the quasi-static compliance experiment [8]), the elastic force is related to the chamber pressure as, $F_c = A_c p_c$, leading to the following equation,

$$\frac{\beta_{C3}}{A_c^3}F_c^3 + \frac{\beta_{C2}}{A_c^2}F_c^2 + \frac{\beta_{C1}}{A_c}F_c + \beta_{C0} = V_{c0} + A_c y_c. \tag{16}$$

This equation must be solved for $F_c(y_c)$ to characterize the spring, which yields three solutions. The real-valued solution is given by the following, while the meaning of the complex-valued solutions is left for future study,

$$F_c(y_c) = G_5(y_c) - \frac{G_1 - G_2^2}{G_5(y_c)} - G_2, \tag{17a}$$

substituting the following G terms for brevity,

$$G_0 = \frac{(\beta_{C0} - V_{c0})A_c^3}{2\beta_{C3}}, G_1 = \frac{\beta_{C1}A_c^2}{3\beta_{C3}}, G_2 = \frac{\beta_{C2}A_c}{3\beta_{C3}}, \tag{17b,c,d}$$

$$G_3 = \frac{\beta_{C1}\beta_{C2}A_c^3}{6\beta_{C3}^2}, G_4(y_c) = G_0 + G_2^3 - G_3 - \frac{A_c^4}{2\beta_{C3}}y_c, \tag{17e,f}$$

$$G_5(y_c) = \left(\sqrt{G_4(y_c)^2 + (G_1 - G_2^2)^3} - G_4(y_c)\right)^{1/3}. \tag{17g}$$

The nonlinear stiffness of the pumping chamber is given by,

$$k_c(y_c) = \frac{F_c(y_c)}{y_c}. \tag{18}$$

The above expression would not be used as such in the simulation since it contains a singularity at $y_c = 0$. Rather, the $k_c(y_c)y_c$ product is always used together, such that $k_c(y_c)y_c|_{y_c=0} = F_c(0) = A_c p_0$, where p_0 is the static pressure in the chambers when the device is at rest. For this example case, p_0 equals one atmospheric plus a small positive pressure which results from the assembly process. The equivalence may be mathematically verified at the element level by simply evaluating,

$$V_c\left(\frac{F_c(y)}{A_c}\right) - V_{c0} - A_c y = 0. \tag{19}$$

In addition, a nonlinear dry friction element is added to capture the amplitude dependence in chamber damping. Although fractional calculus based damping elements capture viscoelastic effects, $D_t^{\alpha_c}(\cdot)$ is a linear operator and therefore will not exhibit amplitude dependence except by interacting with other, nonlinear elements. Many definitions exist for "smoothened" or "soft" friction laws, which affect the dynamic properties [11]. For simplicity, a smoothened kinetic friction element is employed in parallel with the fractional damping element,

$$g_c(y, \dot{y}) = \eta_c D_t^{\alpha_c} y + \mu_c \tanh(\sigma_c \dot{y}), \tag{20}$$

where the friction coefficient is μ_c and the smoothing (regularizing) factor is σ_c. The friction element is nonlinear and directly exhibits amplitude sensitive behavior as well as capturing hysteresis effects that are not described by the viscoelastic terms. The unique effects of frictional and fractional damping elements will be discussed in Section 6.

5.2. Numerical simulation

Numerical solution of the nonlinear model IV is accomplished using a 4th order Runge-Kutta (RK4) numerical integration algorithm [20]. This method solves the initial value problem,

$$\dot{z} = g(t_n, z_n), \quad z(t_0) = z_0, \tag{21a,b}$$

using the following increments (κ_{jn}) at each time-step (n) where z is the state and h is the step time:

$$\kappa_{1n} = g(t_n, z_n), \tag{22a}$$

$$\kappa_{2n} = g\left(t_n + \frac{h}{2}, z_n + \frac{h}{2}\kappa_{1n}\right), \tag{22b}$$

$$\kappa_{3n} = g\left(t_n + \frac{h}{2}, z_n + \frac{h}{2}\kappa_{2n}\right), \tag{22c}$$

$$\kappa_{4n} = g(t_n + h, z_n + h\kappa_{3n}), \tag{22d}$$

$$t_{n+1} = t_n + h, \tag{22e}$$

$$z_{n+1} = z_n + \frac{h}{6}(\kappa_{1n} + 2\kappa_{2n} + 2\kappa_{3n} + \kappa_{4n}). \tag{22f}$$

The time resolution is defined in terms of the desired number of points per period, N_h, and the excitation frequency, Ω in rad/s. Step time is calculated as,

$$h = \frac{2\pi}{\Omega N_h}. \tag{23}$$

Given the simplifying assumptions stated in Section 2, the governing equations may be rewritten as,

$$\dot{y}_1 = \frac{A_x\dot{x} - q_i}{A_c}, \tag{24a}$$

$$\dot{y}_2 = -\frac{A_x\dot{x} - q_i}{A_c}, \tag{24b}$$

$$p_1 = \frac{1}{A_c}\left(k_c(y_1)y_1 + \eta_c D_t^{\alpha_c}[y_1] + \mu_c \tanh(\sigma_c\dot{y}_1)\right), \tag{24c}$$

$$p_2 = \frac{1}{A_c}\left(k_c(y_2)y_2 + \eta_c D_t^{\alpha_c}[y_2] + \mu_c \tanh(\sigma_c\dot{y}_2)\right), \tag{24d}$$

$$\dot{q}_i = \frac{1}{I_i}\left(p_1 - p_2 - R_i(q_i)q_i\right). \tag{24e}$$

The state vector is $\{y_1, y_2, q_i\}^T$ since the pressures are not calculated from the differential equations and therefore do not require integration.

The significance of the simplifying assumptions made in Section 4 ($C_f = 0$, $m_c = 0$) is highlighted by consideration of the expanded state vector, which would become $\{y_1, \dot{y}_1, y_2, \dot{y}_2, p_1, \dot{p}_1, p_2, \dot{p}_2, q_i\}^T$ without these assumptions. The reduction in dimension from 9 to 3 speeds up the algorithm to some extent, but the principal benefit lies in the reduction from second-order system type behavior to the first order type system dynamics. With nonzero chamber wall mass, oscillatory behavior emerges in the y_1 and y_2 states which compromises the numerical stability of the simulation. This is due to numerical "stiffness" [21,22] which arises (in this case) from a wide range of local eigenvalues of the Jacobian matrix. Here, the eigenvalues are dependent on the selected value of non-zero m_c. The numerical stiffness imposes severe restrictions on the step size, which tends to interfere with an efficient computation of fractional derivatives as well as the overall calculation time. Two options are available to overcome the numerical stability problem. The first option would be to add numerical damping to stabilize the second-order systems across varying amplitudes and frequencies [23]. However, this option is not utilized since such artificial damping parameters may greatly exceed the magnitude of physical damping, thus obscuring the physical dissipation effects. The second option (that is employed in this article) would be to assume that $m_c = 0$ and $C_f = 0$; this resolves the computational difficulties by avoiding the second-order system type dynamics in the pumping chamber subsystems.

The fractional derivatives in equations (24c,d) are calculated using the Grünwald-Letnikov difference equation (7), which has inherent history dependence. Efficiently incorporating this term into the 4th order Runge-Kutta algorithm is non-trivial, and many canned numerical integration solvers would be unable to handle this feature [18]. Typically, implicit solvers are used for stiff systems, but these may be incompatible with a direct application of the Grünwald-Letnikov derivative approximation. With an explicit solver, a single step time can be used in both the integration and fractional derivative algorithms and then the history of the variable can align with previous time-steps of the state vector. This obviates the need for interpolation or estimation of the history, which could substantially slow the algorithm. However, the 4th order Runge-Kutta algorithm evaluates slopes at the midpoints between time-steps for the κ_{2n}, κ_{3n} terms and the endpoint for the κ_{4n} term, requiring a unique specification of the state history for each chamber and for each κ term,

$$\kappa_{1n} : \bar{y} = \{y(t - N_j h), \cdots, y(t - jh), \cdots, y(t)\}, \tag{25a}$$

$$\kappa_{2n} : \bar{y} = \left\{\frac{y(t - N_j h) + y(t + h - N_j h)}{2}, \ldots, \frac{y(t - jh) + y(t + h - jh)}{2}, \ldots, \frac{y(t - h) + y(t)}{2}, y(t) + \frac{h}{2}\kappa_{1n}\right\}, \tag{25b}$$

$$\kappa_{3n} : \bar{y} = \left\{\frac{y(t - N_j h) + y(t + h - N_j h)}{2}, \ldots, \frac{y(t - jh) + y(t + h - jh)}{2}, \ldots, \frac{y(t - h) + y(t)}{2}, y(t) + \frac{h}{2}\kappa_{2n}\right\}, \tag{25c}$$

$$\kappa_{4n} : \bar{y} = \{y(t + h - N_j h), \cdots, y(t + h - jh), \cdots, y(t), y(t) + h\kappa_{3n}\}, \tag{25d}$$

to produce a uniformly sampled history ending at t_n, $t_n + h/2$, or $t_n + h$, respectively. Early in the simulation when $t < N_j h$, this required history extends before the initial condition. In this case, the state is assumed to have been at the initial condition for all $t < t_0$. This would create a contradiction simulating a second order system in state space with nonzero initial conditions since both y and $\dot{y}$ would be included in the state. However, the governing differential equations (24a,b,e) are first order type (ignoring the fractional derivatives in equations (24c,d)). Therefore, the only notable result of this assumption is an artificial transient effect near t_0 which is indistinguishable from the other transients generated by the initial condition.

Since a steady-state harmonic solution is desired, the system is integrated until consecutive periods are identical to within a certain threshold. The amount of time required varies depending on the excitation frequency and initial condition. For this example case, when two consecutive periods of $F_T(t)$ compare with an RMS error of less than 0.1% of the peak-to-peak amplitude, a discrete Fourier transform (DFT) of the final period is taken to find the amplitude and phase of the response at the excitation frequency,

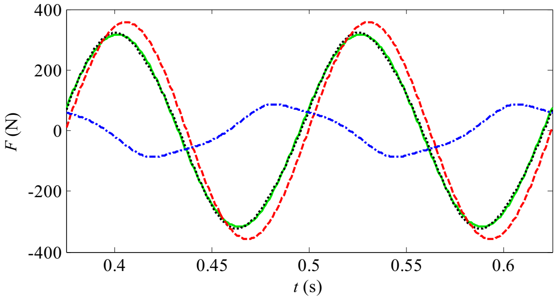

Fig. 5. Predicted time domain response of forces from the nonlinear model IV-1 at 8 Hz with a 2.0 mm peak-to-peak amplitude. Here, F_f exhibits a significantly non-harmonic response, demonstrating the nonlinearity in the system. Key: - - - – F_r; – · – – F_f; ······ – $F_T(t)$ response; —— – $F_T(t)$ sinusoidal fit.

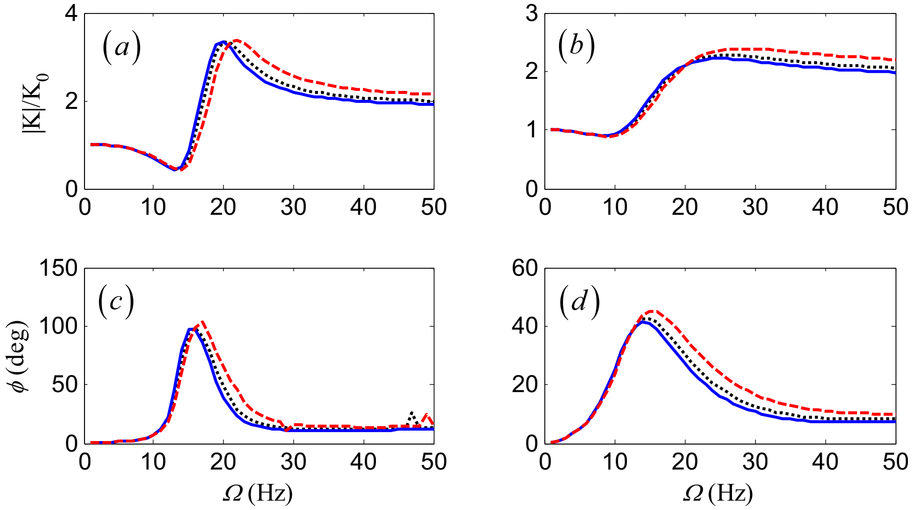

Fig. 6. Effect of fractional damping coefficient (η_c) on the dynamic stiffness magnitude at (a) 0.1 mm and (b) 2.0 mm peak-to-peak excitation and loss angle at (c) 0.1 mm and (d) 2.0 mm peak-to-peak excitation. Key: ······ – baseline η_c; —— – $\eta_c/2$; - - - – $2\eta_c$.

$$\tilde{F}_T(\Omega) = \frac{1}{N_h}\sum_{n=1}^{N_h} F_T(nh)e^{i\Omega nh}, \tag{26}$$

where the overhead tilde represents a complex-valued quantity. Fig. 5 shows an example of the simulated response, comparing the DFT sinusoidal fit with the total response and illustrating the fluid and rubber constituents. The force transmitted through the fluid path exhibits a relatively non-sinusoidal waveform, indicating relatively high harmonic distortion. However, the sinusoidal approximation of the total force (combining rubber and fluid constituents) achieves a high degree of accuracy at all amplitudes and frequencies (suggesting a much lower harmonic distortion) and is used in the calculation of the dynamic stiffness,

$$\tilde{K}_{II}(\Omega) = \frac{\tilde{F}_T(\Omega)}{x_a}. \tag{27}$$

It would also be possible to analytically examine the transmitted force superharmonics, but this is left to future work since the amplitudes are relatively small compared to the first harmonic.

6. Sensitivity of fractional and friction damping parameters

6.1. Fractional damping parameters

Two fractional damping parameters have been introduced to model IV (η_c, α_c), and their effects on the dynamic properties of the system must be understood. To this end, a sensitivity study is carried out, showing the effect of each damping parameter on the dynamic stiffness at each excitation amplitude. Fig. 6 shows the effect of parameter η_c on the

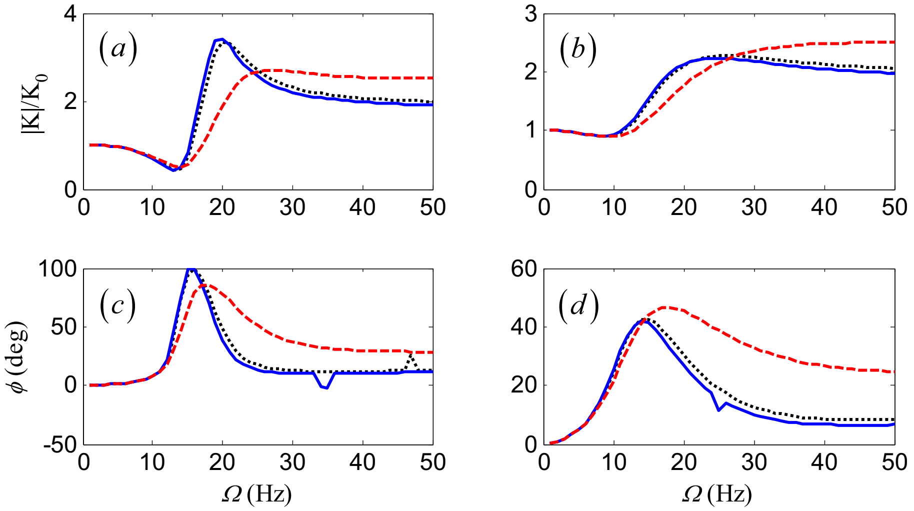

Fig. 7. Effect of fractional damping order (α_c) on the dynamic stiffness magnitude at (a) 0.1 mm and (b) 2.0 mm peak-to-peak excitation and loss angle at (c) 0.1 mm and (d) 2.0 mm peak-to-peak excitation. Key: ⋯⋯ – baseline α_c; —— – $\alpha_c/2$; - - - – $2\alpha_c$.

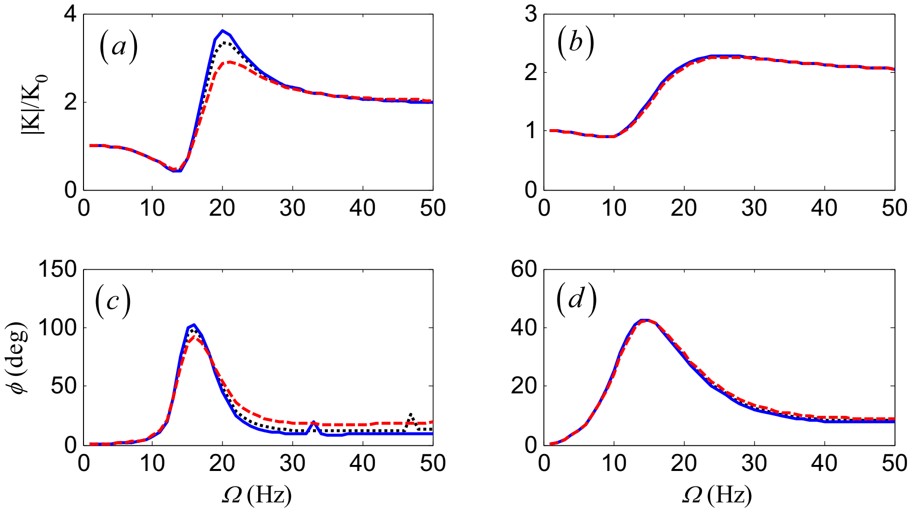

Fig. 8. Effect of dry friction coefficient (μ_c) on the dynamic stiffness magnitude at (a) 0.1 mm and (b) 2.0 mm peak-to-peak displacement and loss angle at (c) 0.1 mm and (d) 2.0 mm peak-to-peak excitation. Key: ⋯⋯ – baseline μ_c; —— – $\mu_c/2$; - - - – $2\mu_c$.

dynamic stiffness magnitude and loss angle for both a small and large amplitude excitation. Several insights emerge. First, the effect is insensitive to excitation amplitude, as expected. For both cases, the loss angle is raised slightly and the dynamic stiffness magnitude increases at frequencies beyond the peak frequency (when the loss angle is maximum). Additionally, a stiffening effect is observed in both the magnitude and phase spectra due to the combined stiffness and damping effects present in a fractional derivative based element. Fig. 7 shows the effect of α_c, which is also similar for each amplitude. A factor of 2 decrease in α_c produces a minimal effect at both amplitudes, while doubling the parameter significantly flattens the peak in stiffness magnitude and substantially increases the loss angle at higher frequencies. This effect is predictable given the nature of the fractional element and limiting cases, where the baseline value of $\alpha_c = 0.3$ represents light damping. As $\alpha_c \to 0$, the fractional damper becomes more like a spring element, but the coefficient η_c is much smaller than the elastic spring coefficient k_c, so any resulting effect is minimal. On the other hand, the limiting case as $\alpha_c \to 1$ is a purely dissipative viscous damper (physically distinct from the elastic element) and thus produces a more significantly different effect.

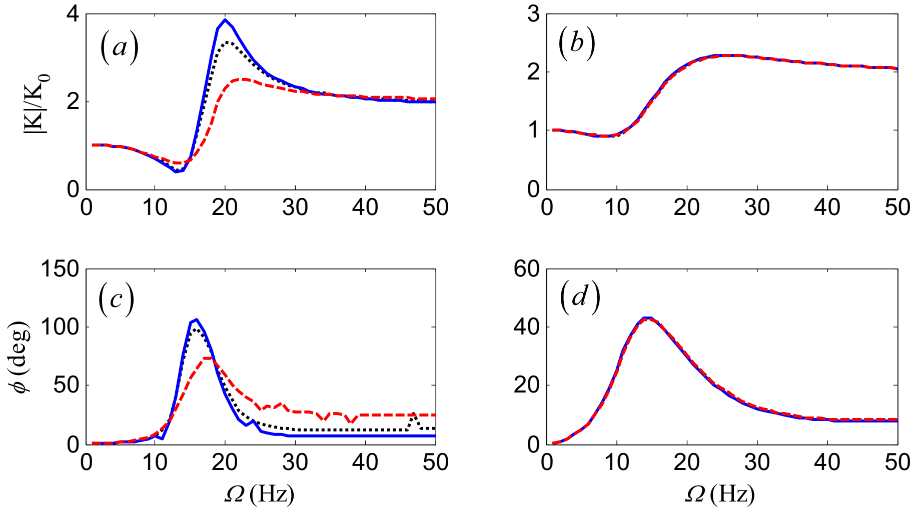

Fig. 9. Effect of friction smoothing coefficient (σ_c) on the dynamic stiffness magnitude at (*a*) 0.1 mm and (*b*) 2.0 mm peak-to-peak excitation and loss angle at (*c*) 0.1 mm and (*d*) 2.0 mm peak-to-peak excitation. Key: ······ – baseline σ_c; —— – $\sigma_c/10$; – – – – $10\mu_c$.

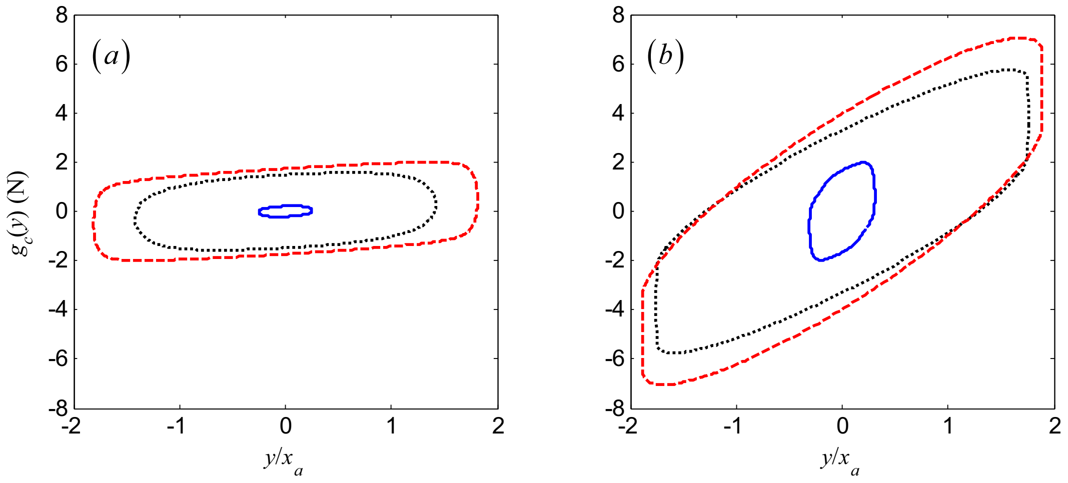

Fig. 10. Predicted dissipation force–displacement (dynamic hysteresis type) curves of the chamber given by, $g_r(y)$ at (*a*) 0.1 mm and (*b*) 1.0 mm peak-to-peak displacement excitation. Key: —— – Ω = 8 Hz; ······ – Ω = 16 Hz; – – – – Ω = 32 Hz.

6.2. Friction damping parameters

The sensitivity of the two dry friction parameters is also of interest, particularly since the behavior of a nonlinear element may be less intuitive than with the linear fractional dampers. Fig. 8 displays the effect of increasing or decreasing μ_c by a factor of 2. The plots demonstrate substantial amplitude dependence since the 2.0 mm simulation shows virtually no sensitivity to the μ_c parameter, while the 0.1 mm dynamic stiffness magnitude is strongly affected near its peak in the spectrum. Similarly, altering the σ_c parameter by a factor of 10 only affects the low amplitude results to any significant degree, as seen in Fig. 9. Here, the peaks in dynamic stiffness magnitude and loss angle spectra decrease with a higher value of σ_c, but the loss angle increases substantially at frequencies beyond the peak frequency. This behavior results directly from the local amplitude sensitivity of the dry friction element. In other words, the particular behavior which exists at amplitudes near a certain operating point is not representative of the global behavior at all amplitudes. This is illustrated in Fig. 10, which presents a force displacement curve across the chamber damping elements at three frequencies and two amplitudes. It is clear that the friction element induces substantially different behavior at alternate excitation amplitudes.

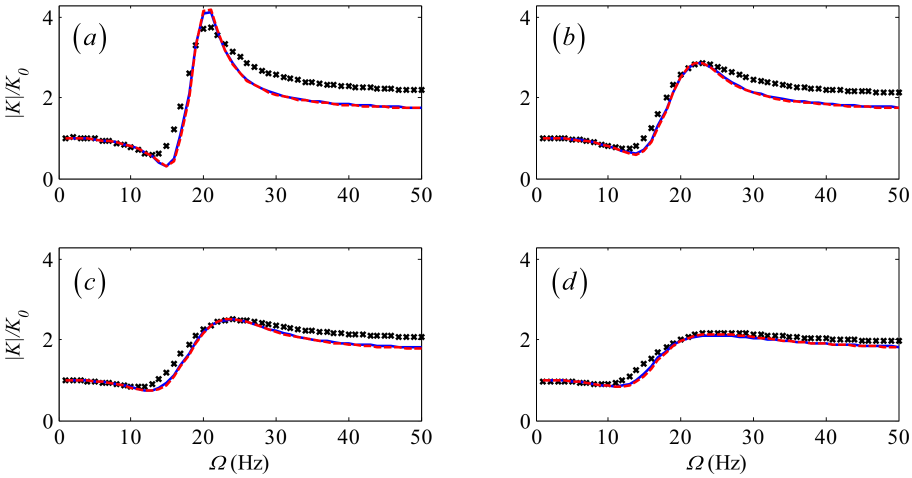

Fig. 11. Dynamic stiffness magnitude of nonlinear models III and IV-0 compared with measurement at (*a*) 0.1 mm, (*b*) 0.5 mm, (*c*) 1.0 mm, and (*d*) 2.0 mm peak-to-peak excitation amplitude. Model IV-0 matches model III, verifying the equivalent nonlinear spring element. Key: × – measurement; —— – model III [1]; - - - – model IV-0.

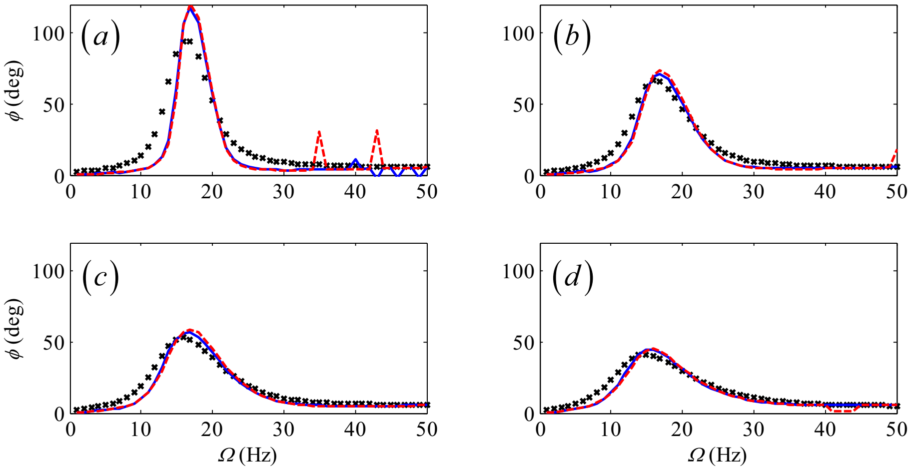

Fig. 12. Loss angle of nonlinear models III and IV-0 compared with measurement at (*a*) 0.1 mm, (*b*) 0.5 mm, (*c*) 1.0 mm, and (*d*) 2.0 mm peak-to-peak excitation amplitude. Model IV-0 matches model III, verifying the equivalent nonlinear spring element. Key: × – measurement; —— – model III [1]; - - - – model IV-0.

7. Experimental validation and computational verification of new nonlinear models

Model IV is verified (as model IV-0) by using the same parameters as model III [1], so the only differences would be in the integration algorithms used. Figs. 11 and 12 compare the model IV-0 dynamic stiffness spectra with the spectra of model III given previously [1] and the measurement, showing virtually complete agreement, as expected. Two minor discrepancies justify some discussion. First, the loss angle spectra near the peaks show a small discrepancy between the two nonlinear models. This is due to the fact that a different phase estimation algorithm was employed in model IV (DFT) vs. model III (least squares regression). The new DFT algorithm is more precise, whereas the resolution of the regression method was directly dependent on N_h. Second, small peaks exist in the loss angle spectra at higher frequencies, particularly at the 0.1 mm amplitude. These are numerical artifacts of the integration algorithm and the errors may be reduced by enhanced resolution but at the cost of increased computational time. For most practical purposes these errors may simply be ignored. The new model has more of these erroneous points than the former since the 4th order Runge-Kutta algorithm uses a fixed step whereas the previous method allowed for an adaptive step size [1], and thus would require lower resolution.

Having successfully reproduced the results of [1], a new parameter set can be employed with model IV-1 to improve its predictive accuracy compared with measured dynamic stiffness spectra. Figs. 13 and 14 show the resulting dynamic stiffness

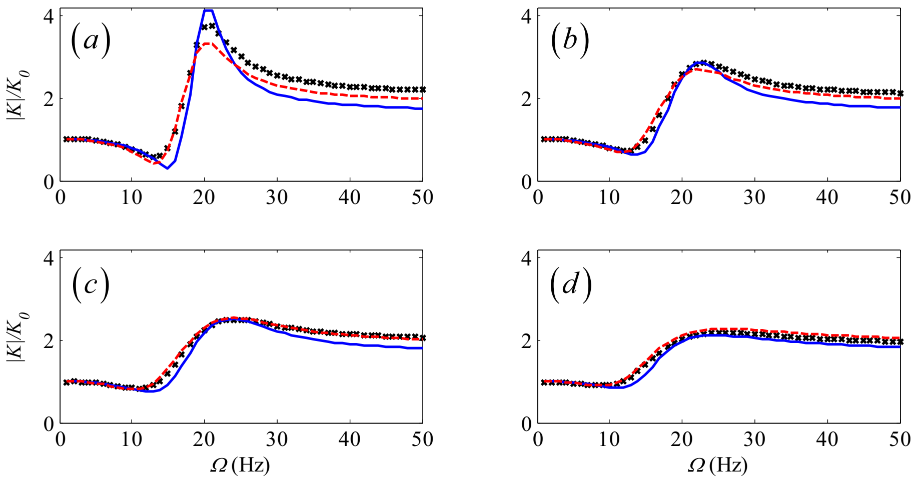

Fig. 13. Dynamic stiffness magnitude of nonlinear models at (*a*) 0.1 mm, (*b*) 0.5 mm, (*c*) 1.0 mm, and (*d*) 2.0 mm peak-to-peak excitation amplitude. Model IV-1 shows improved accuracy compared with model III indicating the importance of chamber damping in predictions of dynamic amplitude sensitivity. Key: × – measurement; —— – model III [1]; - - - – model IV-1.

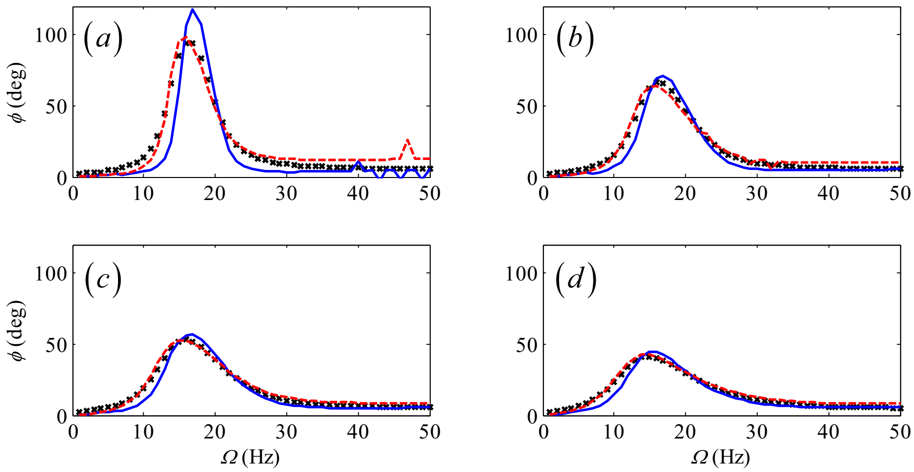

Fig. 14. Loss angle of nonlinear models at (*a*) 0.1 mm, (*b*) 0.5 mm, (*c*) 1.0 mm, and (*d*) 2.0 mm peak-to-peak excitation amplitude. Model IV-1 shows improved accuracy compared with model III indicating the importance of chamber damping in predictions of dynamic amplitude sensitivity. Key: × – measurement; —— – model III [1]; - - - – model IV-1.

magnitude and loss angle with nonzero fractional and friction damping in the pumping chambers. Observe that model IV-1 achieves improved accuracy over model III at all amplitudes in terms of both magnitude and phase. This demonstrates that the inclusion of compliance chamber damping terms provides necessary dynamic interaction(s) with the other nonlinear features to accurately predict the bushing's response over a range of excitation amplitudes. Additional insights are obtained from a careful examination of the magnitude spectra across the range of amplitudes. In particular, model IV-1 tends to under-predict $|\tilde{K}_{IV}|$ at the lower excitation amplitudes, and over-predict it at the higher ones, balancing with an excellent prediction near 1.0 mm. Since the over/under-prediction vs. amplitude relationship appears nearly linear, it would suggest that at least one amplitude-dependent parameter is being linearized in model IV.

It has been previously suggested [1,8] that a nonlinear characterization of pumping area might improve model accuracy. Therefore, a quasi-linear $A_x(x_a)$ parameter is numerically introduced to conceptually demonstrate the potential effectiveness of model IV with limited further refinement. Figs. 15 and 16 depict the resulting stiffness magnitude and phase spectra, showing excellent agreement at all amplitudes. Table 4 compares the RMS error of each nonlinear model, showing a general improvement over model III and exceptional accuracy with model IV-2, particularly at the higher amplitudes where the error is reduced by over half. This suggests a clear need to characterize the physical (and complicated) nature of $A_x(x)$ in future studies.

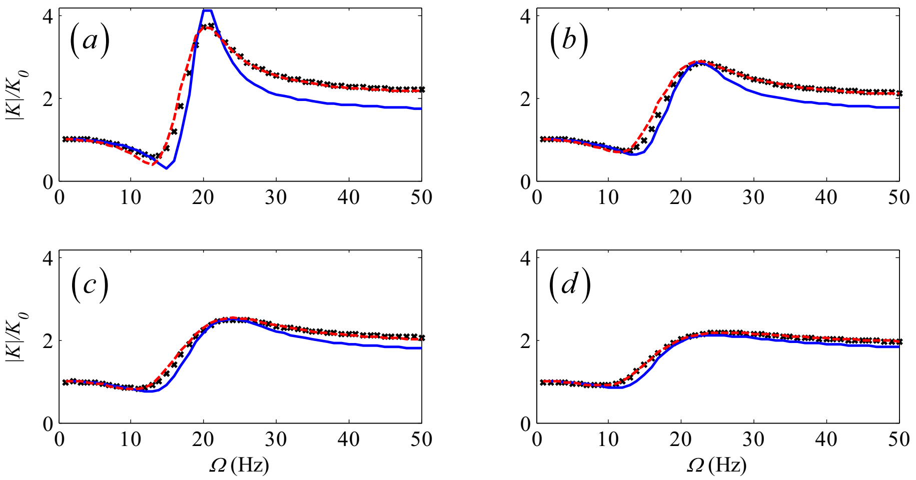

Fig. 15. Dynamic stiffness magnitude of nonlinear models with quasi-linear $A_x(x_a)$ at (a) 0.1 mm, (b) 0.5 mm, (c) 1.0 mm, and (d) 2.0 mm peak-to-peak excitation amplitude. Model IV-2 achieves a substantial improvement in accuracy over model III when compared with the measurement, suggesting that the amplitude sensitivity of the A_x parameter is also significant to the nonlinear dynamics. Key: × – measurement; —— – model III [1]; - - - – model IV-2.

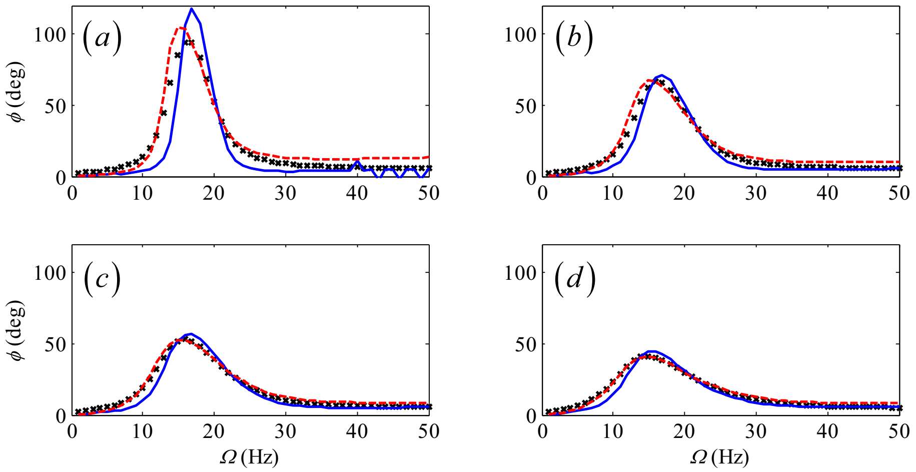

Fig. 16. Loss angle of nonlinear models with quasi-linear $A_x(x_a)$ at (a) 0.1 mm, (b) 0.5 mm, (c) 1.0 mm, and (d) 2.0 mm peak-to-peak excitation amplitude. Model IV-2 achieves a substantial improvement in accuracy over model III when compared with the measurement, suggesting that the amplitude sensitivity of the A_x parameter is also significant to the nonlinear dynamics. Key: × – measurement; —— – model III [1]; - - - – model IV-2.

Table 4
Error of the new nonlinear models with respect to measured dynamic stiffness spectra. Each new model (IV-1 or IV-2) achieves a substantial improvement.

Model	RMS error at peak-to-peak amplitude (x_a)			
	0.1 mm	0.5 mm	1.0 mm	2.0 mm
Model III, from [1]	49.28%	28.31%	19.16%	12.92%
Model IV-1	28.94%	15.86%	7.99%	10.59%
Model IV-2	21.84%	13.75%	7.99%	6.10%

8. Conclusion

This article significantly extends the prior article [1] by incorporating new damping elements in amplitude sensitive, nonlinear hydraulic bushing models under steady state harmonic excitation up to 50 Hz between 0.1 and 2.0 mm peak-to-peak amplitudes. Fractional calculus viscoelastic elements as well as smoothened dry friction dampers have been introduced to the fluid pumping chambers; new models capture unique dynamic behavior which is beyond the nonlinear dissipative elements used in prior models [1,7,8]. Careful assessments of new or improved empirical quasi-linear and analytical nonlinear models reveal that the fractional calculus viscoelasticity contributes a necessary, or at least appropriate, influence on the linearized and amplitude sensitive dynamics, respectively. In particular, the fractional order transfer functions of model II reduce the RMS error of model I by 77%, averaged across all amplitudes. Nonlinear model IV-1 reduces the RMS error of model III by 40%, demonstrating not only significant improvement, but superior predictive performance than even a curve-fit of measured data under the formulation of prior work [1].

Overall, this article identifies new, significant, amplitude sensitive damping elements in a typical hydraulic bushing and proposes an analytical technique (based on fractional calculus) to accurately simulate its dynamic behavior. In particular, this article offers three distinct contributions to the state of the literature. First, improved quasi-linear models which include fractionally damped pumping chambers substantially reduce the RMS error in dynamic stiffness at all amplitudes compared with the prior work [1], suggesting that proposed model features are indeed relevant in terms of linearized system dynamics. Second, new nonlinear models exhibit accurate amplitude sensitive behavior which matches very well with dynamic stiffness measurements at multiple excitation amplitudes, suggesting a reasonable and nuanced characterization of the physics. Third, experimental validation of both quasi-linear and nonlinear models at several amplitudes lends credence to physical insights derived from these models, such as the observed interactions between the new damping elements and other nonlinear elements in the system or the need to characterize the nonlinear nature of the A_x parameter. The proposed models could be extended to other hydraulic devices [24].

The scope of this article has been limited to uniaxial, steady-state harmonic excitation up to 50 Hz with 0.1, 0.5, 1.0, and 2.0 mm peak-to-peak excitation amplitudes. Physical effects not included in the new models (II, IV) may become dominant in other loading directions, or beyond the 2.0 mm amplitude, or at a higher frequency range. For example, a nonlinear stiffness element (stopper) would engage at very high amplitudes, altering the dynamic properties substantially. Additionally, internal resonances of both the rubber material and fluid system would be observed at very high frequencies (say around 1 kHz) [12,13], and thus the lumped parameter modeling framework [1–8] would be inadequate. Finally, this article suggests the need for improved characterization of pumping area, (A_x) as it indeed exhibits amplitude sensitivity. A new experimental study (perhaps similar to the fluid compliance experiment of [8]) would be needed to better characterize the nonlinear behavior of $A_x(x, p)$.

Acknowledgement

We acknowledge the member organizations of the Smart Vehicles Concepts Center (www.SmartVehicleCenter.org) such as Transportation Research Center Inc., Honda R&D Americas, Inc., F.tech R&D North America, Inc., Tenneco, Inc., Ford Motor Company, and the National Science Foundation Industry/University Cooperative Research Centers program (www.nsf.gov/eng/iip/iucrc) for supporting this work.

Appendix A. List of symbols

A	effective pumping area (m^2)
B	transfer function coefficient
C	fluid compliance (m^5/N)
D	derivative operator
F	force (N)
G	elastic model parameter
g	damping forcing function (N·s/m)
h	time step (s)
I	fluid inertance ($\text{N}\cdot\text{s}^2/\text{m}^5$)
j	fractional derivative history term index
K	dynamic stiffness (N/m)
k	elastic spring coefficient (N/m)
$\mathcal{L}$	Laplace transform
m	effective mass (kg)
N	number of terms
n	time step index
p	pressure (Pa)
q	volume flow rate (m^3/s)
R	fluid resistance ($\text{N}\cdot\text{s}/\text{m}^5$)
s	Laplace domain variable (1/s)
t	time (s)

V	volume (m^3)
X	displacement of inner sleeve in the Laplace domain (m)
x	displacement of inner sleeve in the time domain (m)
y	effective displacement of pumping chamber wall (m)
Z	arbitrary displacement in Laplace domain (m)
z	arbitrary displacement in time domain (m)
α	fractional derivative order
β	model parameter
Γ	the gamma function
ε	root mean squared error
η	fractional/viscous damping coefficient
κ	Runge-Kutta increment
μ	friction coefficient (N)
ξ	empirical correction factor
σ	smoothing factor (1/s)
τ	variable of integration (s)
ϕ	loss angle (rad)
Ω	excitation frequency (rad/s)

Subscripts

0	initial or static value
1, 2	pumping chambers 1 and 2
a	amplitude (peak-to-peak)
c	compliance chamber
f	fluid path
i	inertia track
M	measured
r	rubber path
T	total transmitted force

Superscripts

–	history
∼	complex-valued variable

Abbreviations

DFT	discrete Fourier transform
NL	nonlinear
RMS	root mean squared
QL	quasi-linear

References

[1] L. Fredette, J.T. Dreyer, T.E. Rook, R. Singh, Harmonic amplitude dependent dynamic stiffness of hydraulic bushings: alternate nonlinear models and experimental validation, Mech. Syst. Signal Process. 75 (2016) 589–606, https://doi.org/10.1016/j.ymssp.2015.11.017.

[2] N. Gil-Negrete, A. Rivas, J. Vinolas, Predicting the dynamic behaviour of hydro bushings, Shock Vib. 12 (2005) 91–107, https://doi.org/10.1155/2005/748498.

[3] S. Arzanpour, M. Golnaraghi, Development of a bushing with an active compliance chamber for variable displacement engines, Vehicle Syst. Dyn. 46 (2008) 867–887, https://doi.org/10.1080/00423110701683134.

[4] T. Chai, J.T. Dreyer, R. Singh, Time domain responses of hydraulic bushing with two flow passages, J. Sound Vib. 333 (2014) 693–710, https://doi.org/10.1016/j.jsv.2013.09.037.

[5] T. Chai, J.T. Dreyer, R. Singh, Frequency domain properties of hydraulic bushing with long and short passages: system identification using theory and experiment, Mech. Syst. Signal Process. 56 (2015) 92–108, https://doi.org/10.1016/j.ymssp.2014.11.003.

[6] M. Sevensson, M. Hakansson, Hydrobushing model for multi-body simulation (M.S.thesis), Lund University, Lund, Sweden, 2004.

[7] T. Chai, J.T. Dreyer, R. Singh, Nonlinear dynamic properties of hydraulic suspension bushing with emphasis on the flow passage characteristics, Proc. IMechE Part D: J. Automob. Eng. (2014), https://doi.org/10.1177/0954407014561048.

[8] L. Fredette, J.T. Dreyer, R. Singh, Dynamic analysis of hydraulic bushings with measured nonlinear compliance parameters, SAE Int. J. Passeng. Cars - Mech. Syst. 8 (2015) 2015-01-2355. http://doi.org/10.4271/2015-01-2355.

[9] R. Herrmann, Fractional Calculus: An Introduction for Physicists, World Scientific Publishing Co., Singapore, 2014.

[10] Y. Rossikhin, M. Shitikova, Applications of fractional calculus to dynamic problems of linear and nonlinear hereditary mechanics of solids, J. Appl. Mech.-T. ASME. 50 (1997) 15–67, https://doi.org/10.1115/1.3101682.

[11] M. Sjoberg, L. Kari, Nonlinear isolator dynamics at finite deformations: an effective hyperelastic, fractional derivative, generalized friction model, Nonlinear Dyn. 33 (2003) 323–336 http://doi.org/10.1023/A:1026037703124.

[12] L. Fredette, R. Singh, Estimation of the transient response of a tuned, fractionally damped elastomeric isolator, J. Sound Vib. 382 (2016) 1–12, https://doi.org/10.1016/j.jsv.2016.07.009.

[13] L. Fredette, R. Singh, High frequency, multi-axis dynamic stiffness analysis of a fractionally damped elastomeric isolator using continuous system theory, J. Sound Vib. 389 (2017) 468–483, https://doi.org/10.1016/j.jsv.2016.11.025.

[14] R.L. Bagley, P.J. Torvik, A theoretical basis for the application of fractional calculus to viscoelasticity, J. Rheol. 27 (1983) 201–210, https://doi.org/10.1122/1.549724.

[15] J. Wu, W. Shangguan, Modeling and applications of dynamic characteristics for rubber isolators using viscoelastic fractional derivative model, J. Eng. Mech. 25 (2008) 161–166.

[16] W. Sauer, Y. Guy, Hydro bushings-innovative NVH solutions in chassis technology, SAE Technical Paper 2003-01-1475, 2003 http://doi.org/10.4271/2003-01-1475.

[17] B. Piquet, C. Maas, F. Capou, Next generation of suspension bushings: review of current technologies and expansion upon new 3rd generation product data. SAE Technical Paper 2007-01-0850, 2007 http://doi.org/10.4271/2007-01-0850.

[18] M.A.T.L.A.B. Release, The MathWorks Inc, Natick, Massachusetts, United States, 2013.

[19] E. Wylie, V. Streeter, Fluid Transients, McGraw-Hill, 1978.

[20] W.H. Press, S.A. Teukolski, W.T. Vetterling, B.P. Flannery, Numerical Recipes in FORTRAN, second ed., Cambridge University Press, UK, 1992.

[21] C. Padmanabhan, R.C. Barlow, T.E. Rook, R. Singh, Computational issues associated with gear rattle analysis, J. Mech. Des. 117 (1995) 185–192, https://doi.org/10.1115/1.2826105.

[22] R.C. Aiken (Ed.), Stiff Computation, Oxford University Press, New York, Oxford, 1985.

[23] H. Hilber, T. Hughes, R. Taylor, Improved numerical dissipation for time integration algorithms in structural dynamics, Earthquake Eng. Struct. D 5 (1977) 283–292, https://doi.org/10.1002/eqe.4290050306.

[24] H. Marzbani, R. Jazar, M. Fard, Hydraulic engine mounts: a survey, J. Vib. Control 20 (2014) 1439–1463, https://doi.org/10.1177/1077546312456724.